

A Low Frequency Survey of Giant Pulses  
from the Crab Pulsar

Tarraneh Eftekhari

*Department of Physics & Astronomy  
University of New Mexico, Albuquerque, NM 87131*

December 2, 2014

# A Low Frequency Survey of Giant Pulses from the Crab Pulsar

## Contents

<b>1</b>	<b>Introduction</b>	<b>1</b>
1.1	History . . . . .	1
1.2	Giant Radio Pulses . . . . .	2
<b>2</b>	<b>Pulsars</b>	<b>2</b>
2.1	Pulsar Magnetosphere . . . . .	2
2.2	Main Pulse and Interpulse . . . . .	4
2.3	Dispersion & Scattering . . . . .	6
2.4	Pulsar Glitches . . . . .	9
<b>3</b>	<b>Emission Mechanism</b>	<b>10</b>
3.1	High Energy Radiation . . . . .	11
3.2	Giant Radio Pulses . . . . .	11
<b>4</b>	<b>Data Analysis</b>	<b>13</b>
4.1	Instrumentation – LWA1 . . . . .	13
4.2	Observations . . . . .	13
4.3	Data Reduction . . . . .	14
4.4	Identification of Giant Pulses . . . . .	14
4.5	Flux Calibration . . . . .	15

<b>5</b>	<b>Results &amp; Discussion</b>	<b>17</b>
5.1	Occurrence of Giant Radio Pulses . . . . .	17
5.2	Variations in DM . . . . .	18
5.3	Characteristic Broadening Time . . . . .	19
<b>6</b>	<b>Conclusion and Future Work</b>	<b>24</b>

## 1. Introduction

### 1.1. History

At the center of the Crab Nebula, a distance of 2200 pc away, lies a rapidly rotating neutron star, the Crab Pulsar (B0531+21). The supernova responsible for the subsequent nebula was first witnessed on July 4, 1054 by Chinese astronomers and was documented as having remained visible for a period of 642 days. In 1754, Carl Messier observed the Crab Nebula while tracking comets in the sky, incidentally the same year in which Comet Halley would make its prophetic debut. He would soon after note the existence of 100 other nebulae and categorize them all within what would become the Messier Catalog. The Crab Nebula would thus hold its distinguished place as the first noted object amongst many in the extensive list of catalog entries that exists today (Mayall 1939).

In 1928, Edwin Hubble observed a notable expansion of the nebula, and by extrapolating the rate of expansion backwards in time, deduced that the progenitor event must have taken place roughly 900 years prior. Given the location of the nebula on the sky, Hubble deduced that in fact the stellar explosion witnessed by Chinese astronomers in 1054 and the resultant nebula were inextricably tied (Mayall 1939).

In 1968, David H. Staelin and Edward C. Reifstein published a paper announcing their discovery of two new pulsating radio sources near the Crab Nebula (Staelin & Reifstein 1968). Using the 90 m Green Bank Telescope in West Virginia, Staelin and Reifstein observed the pulses between 110-115 MHz. Their results allowed them to place an upper limit of 0.15 s on the period of the Crab Pulsar, shedding new light on the source of energy lying at the center of the Crab Nebula.

In this thesis, we present a survey of giant pulses from the Crab Pulsar as observed with the first station of the Long Wavelength Array. Statistical distributions are examined and compared to previous studies at various frequencies. The science behind pulsars and their elusive emission mechanisms are also explored.

## 1.2. Giant Radio Pulses

The emission profile of the Crab exhibits occasional bursts of increased intensity known as Giant Radio Pulses (GRPs). GRPs from the Crab Pulsar can reach flux densities of up to several thousand times the average flux, becoming one of the brightest radio sources in the sky (Jessner et al. 2005). In general, GRPs are defined as having flux densities at least 10 times the average flux density and are characteristically short-lived (on the order of microseconds to nanoseconds) (Hankins & Eilek 2007a). The intensity and energy distributions of GRPs can be modeled by a power-law, whereas the distribution is exponential in the case of regular pulses, which may be indicative of varying emission mechanisms (Karuppusamy et al. 2010).

Although the Crab Pulsar has been observed rather extensively across the electromagnetic spectrum, the specific processes responsible for the emission remain elusive. Furthermore, emission mechanisms have been shown to differ for radiation from different regions of the spectrum. A clearer understanding of the mechanisms that result in giant pulses will help to reveal the overlying nature of pulsars and the curious radiation they emit.

## 2. Pulsars

### 2.1. Pulsar Magnetosphere

The magnetic field of the Crab Pulsar plays an intrinsic role in the radiation that the neutron star emits. Although different forms of radiation emerge from varying locations within the magnetic field, a greater understanding of the induced magnetospheric plasma is necessary in order to begin to understand the emission mechanisms.

For pulsars with high angular velocity  $\boldsymbol{\Omega}$  and strong magnetic fields  $\mathbf{B}$  (such as the Crab, with a period of 0.033 s and a magnetic field of  $3.7 \times 10^{12} G$ ) (Lyutikov 2007), the charge density of the surrounding magnetosphere contained within the light cylinder and bounded by closed magnetic field lines is given by

$$\rho_0 = \nabla \cdot \frac{(\boldsymbol{\Omega} \times \mathbf{r}) \times \mathbf{B}}{4\pi c} \quad (1)$$

henceforth referred to as the Goldreich - Julian density. (The light cylinder is centered about the rotation axis and is defined as the distance at which the corotation speed of the neutron star equals the speed of light (Carroll & Ostlie 2007).) This charge density arises as the magnetic field spins through the neutron star which can itself be thought of as a perfect conductor. Rotation of the magnetic field induces an electric field. The Goldreich - Julian charge density can be obtained by solving Laplace's equation for the electric potential and applying the necessary discontinuous boundary conditions for the normal component of the electric field at the surface of the star (Goldreich & Julian 1969). Subsequently, the steady - state Goldreich - Julian charge density is merely a result of the induced electric field due to the rotation of the dipolar magnetic field. Given large electric fields in the direction of the magnetic field ( $\mathbf{E} \cdot \mathbf{B}$ ), electron-positron pair production can occur, and a pair plasma is induced. The flow of the plasma establishes the charge density  $\rho_0$  throughout the magnetosphere (See Figure 1) (Cheng et al. 1986a).

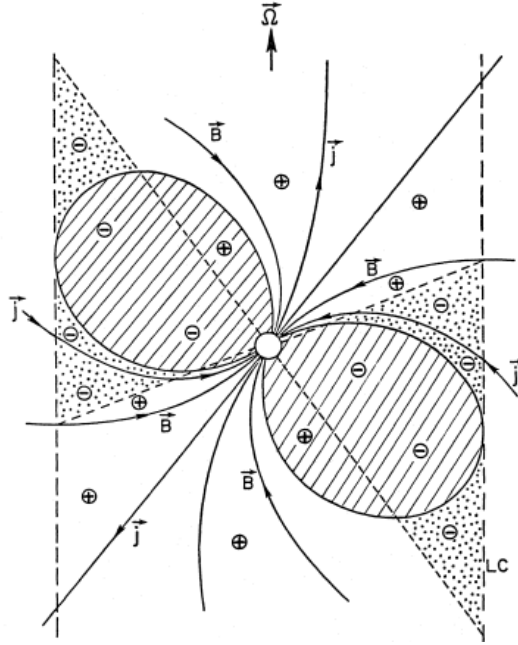


**Fig. 1.**—: Illustration of charge densities in varying regions within the pulsar light cylinder. In the region bounded by closed magnetic field lines, the Goldreich - Julian density  $\rho_0$  exists. In the dotted region, potential differences work to establish  $\rho \sim \rho_0$ . The pair plasma flows along open magnetic field lines (Cheng et al. 1986a).

Coherent radio emission emerges from the plasma filled magnetosphere where the mag-

netic field lines remain open beyond the extent of the light cylinder. As the neutron star rotates about its rotation axis, these open field line regions sweep in and out of our line of sight emitting periodic bursts of radiation. The microstructure of observed giant pulses can elucidate the nature of the plasma in these regions. In particular, high time resolution observations can probe subtle variations in the microstructure of a pulse. Similarly, the width of a giant pulse can be indicative of turbulence within the magnetosphere. Wide bandwidth observations of giant pulses are therefore necessary in order to constrain the frequency dependence of pulse widths (Hankins et al. 2010). If the observed dependence of pulse widths varies from a Kolmogorov spectrum, in which the width (or the characteristic broadening time  $\tau_d$ )  $\propto \nu^{-4.4}$ , it may be that the magnetospheric plasma imparts some intrinsic broadening due to turbulence. The Kolmogorov model describes turbulent motions of homogeneous, isotropic regions and derives the corresponding energy spectrum. The proportionality  $\tau_d \propto \nu^{-4.4}$  is thought to describe the interstellar medium (ISM). Values that deviate from that given by the exponent value of -4.4 are then indicative of passage through a turbulent medium other than the ISM.

## 2.2. Main Pulse and Interpulse

The average pulse profile of the Crab is comprised of a Main Pulse (MP) and Interpulse (IP), the latter of which can be identified across the electromagnetic spectrum, from low radio frequencies up to gamma rays (Hankins & Eilek 2007a). The occurrence of IPs is believed to be a consequence of the nearly orthogonal alignment of the rotational and magnetic axes (Karuppusamy et al. 2010). The differing properties among the two types of pulses suggest varying emission mechanisms. The following section describes the characteristics of both MPs and IPs. As these properties cannot be probed at our frequency range, we provide a brief discussion here.

The MP dominates the spectrum below 5 GHz where giant pulses are most common. MPs are typically characterized by a series of subsequent microbursts, as shown in Figure 2, whose widths are on the order of  $3 - 30\mu\text{s}$ . These microbursts are believed to be composites of several nanoshots (bursts on nanosecond timescales) which are difficult to identify individually due to their short durations and narrow bandwidths, although there have been several

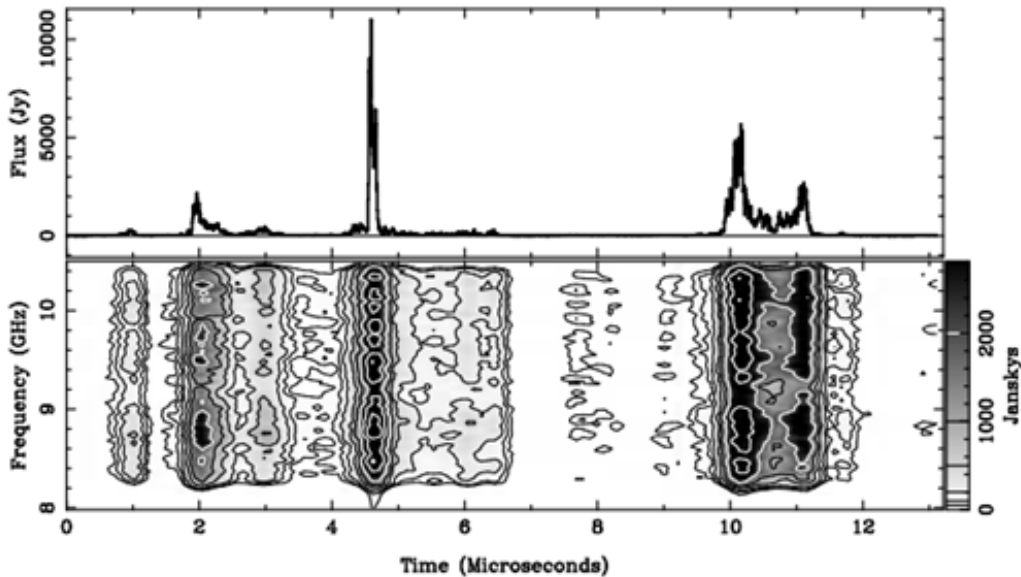


**Fig. 2.**—: A main pulse, observed at 9 GHz with 2.2 GHz bandwidth. Several microbursts are evident. The light curve spans the full bandwidth (Hankins & Eilek 2007a).

reported instances (see Hankins & Eilek 2007a). The properties of microbursts, including their energy and total duration, as well as the number of observed bursts, vary on a pulse-to-pulse basis (Crossley et al. 2010). The occurrence of both microbursts and nanoshots can be perhaps attributed to dissimilarities in magnetospheric plasma densities, such as plasma clumps which can be on the order of approximately 3 m. Alternatively, they may be due to irregularities that arise within the beam of emission from period to period. This particular notion is supported by the fact that microbursts and nanoshots are observed at a rate consistent with the pulsar’s period (Petrova 2004).

Below 1 GHz, the microbursts within the MP profile exhibit a rapid rise followed by a long tail due to scattering by the interstellar medium (ISM). The pulse widths for pulses below 1 GHz are then indicative of the density of the ISM. Above this value, however, the observed pulse is not subject to scattering (Hankins & Eilek 2007a).

The profile of the IPs exhibits less of the symmetric nature of the MPs, and instead is characterized by a rapid rise, diminishing more gradually over time. IPs typically last  $1 - 3\mu\text{s}$  in duration. Secondary pulses can be observed following an IP, where these subsequent pulses

typically overlap with the initial pulse, as shown in Figure 3 (Hankins & Eilek 2007a).

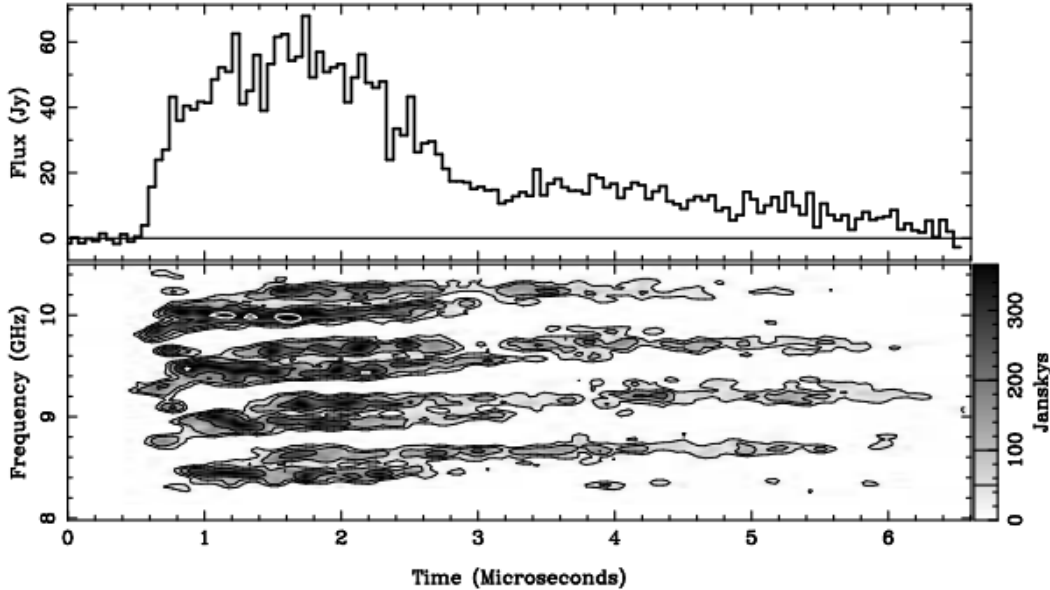


**Fig. 3.**—: An Interpulse, observed at 9 GHz with 2.2 GHz bandwidth. The spectrum is comprised of narrow emission bands that drift slightly upward while maintaining a constant spacing (Hankins & Eilek 2007a).

In general, MPs are broadband in nature, however, several nanoshots have been observed in which the shots do not extend across the entire bandwidth. The broadband nature of MPs is therefore likely not related to the emission process, and instead, an artifact of the overlapping of multiple nanoshots. Conversely, the IP profile is constituted by characteristic emission bands. Emission bands are observed between 5 and 10 GHz. These bands exhibit little deviation from the central frequency over the duration of a pulse, tending slightly upwards. Interestingly, the spacing between adjacent bands is related to the average frequency,  $\Delta v/v = 0.06$ , however this spacing remains fairly constant even as the pulses drift upwards (Hankins & Eilek 2007a).

### 2.3. Dispersion & Scattering

As pulses from the Crab travel through the ISM, the observed pulse is subject to dispersion and scattering as a function of the electron density along the line of sight. The effect

of dispersion is to delay low frequency waves relative to their higher frequency counterparts. The electric field of the emitted radio waves varies as a function of time, which causes the electrons encountered through the ISM to vibrate. The electrons slow the wave, affecting the lower frequency waves to a greater extent (Carroll & Ostlie 2007). The amount of dispersion that occurs is directly related to the integrated column density of electrons along the line of sight from the observer to the pulsar, also known as the dispersion measure (DM) (Stappers et al. 2011). The DM for the Crab Pulsar is  $56.791 \text{ pc}/\text{cm}^3$  (Ellingson et al. 2013a). Figure 4 illustrates the effects of dispersion.

Pulses are also broadened due to scattering as they travel through the ISM. Due to the density of the ISM, a given pulse emitted from the Crab will travel varying geometrical paths. The resultant observed pulse suffers from some apparent broadening. This phenomenon is particularly prevalent at lower frequencies, where the scattering dependence goes as  $\lambda^4$  (Lang 1971).

To explain the effects of scattering here, we adopt the thin slab model (see Figure 5). In this model, a thin slab of electrons exists between the pulsar and observer with a number density of electrons,  $n_e$ , that is changing over time. As a wave traveling from the pulsar passes through the slab, the wave undergoes a phase change due to density fluctuations within the slab. This phase change is given by

$$\Delta\phi = \frac{r_e \Delta n_e a c}{\nu} \quad (2)$$

where  $r_e$  is the classical electron radius,  $a$  is the scale size of a given collection of electrons, and  $\nu$  is the frequency of the passing wave (Lang 1971). If the pulsar is located at a distance  $L$  from the observer, then the root mean square of the angle of scattering is given by

$$\theta_{rms} = \frac{\phi_0 c}{2\pi a \nu} = 4 \times 10^7 \cdot \sqrt{\frac{L}{a} \frac{\sqrt{\langle n_e^2 \rangle}}{\nu^2}} \quad (3)$$

where  $\phi_0$  is the rms value which describes the phase fluctuations (Lang 1971).

For waves traveling at some angle  $\theta$  (as seen by the observer), the arrival time  $\tau$  relative to an unscattered wave is given by

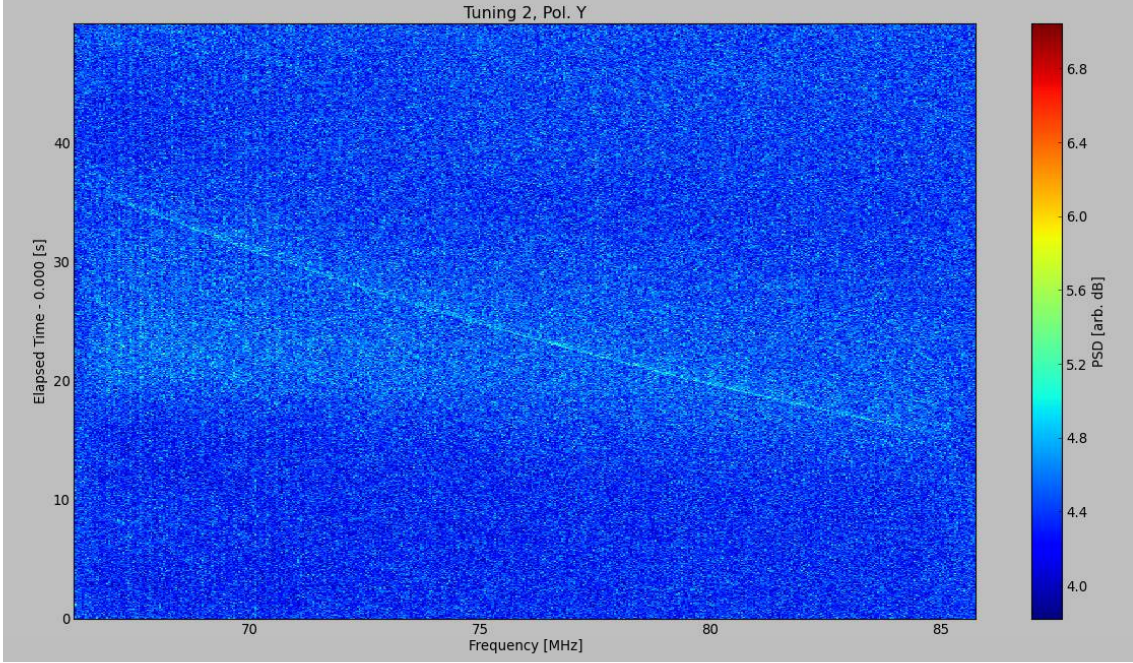


**Fig. 4.—** An example of the effects of dispersion. GRP observed at 76MHz with 16MHz bandwidth. Observed with the Long Wavelength Array. High frequency waves arrive sooner than low frequency waves.

$$\tau = \frac{L\theta^2}{2c(L - R)} \quad (4)$$

where  $R$  is the distance to the scattering slab from the observer (Cronyn 1970). While the head of a traveling wave may arrive at the observer at some time  $\tau$ , the successive portion of the wave arrives at a later time  $\tau + d\tau$ . The total flux arriving between  $\tau$  and  $\tau + d\tau$  is given by integrating the flux over all angles.

$$g(\tau)d\tau = \frac{1}{\tau_d} \exp(-\tau/\tau_d)d\tau \quad (5)$$

where  $\tau_d = L\theta_{rms}^2/2c(L - R)$  (Cronyn 1970).  $\tau_d$  has been known to fluctuate by factors of 2-10 over periods of months. Such variations are likely due to high density clouds within the nebula that pass along the line of sight. We can, for instance, imagine multiple scattering slabs along the line of sight, where some may exist in the environment immediately surrounding the pulsar.  $\tau_d$  therefore depends on the distribution of electrons along the line

of sight, where the DM provides the total integrated number of electrons. Equation 5 gives us the characteristic scattering tail of dispersed pulses, where there is initially a sharp rise, followed by an exponential decay (Ellingson et. al 2013a). Figure 6 illustrates the effects of broadening on a pulse.

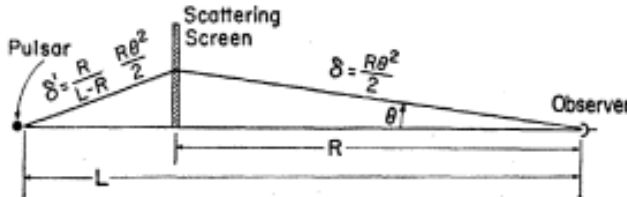


**Fig. 5.**—: Illustrates excess path length traversed by an emitted wave (Cronyn 1970).

For the purposes of this study, we adopt the following equation which has been shown to accurately describe pulses in the lowest frequency range (Karuppusamy et al. 2012):

$$g(t) = t^\beta \exp(-t/\tau_d)u(t) \quad (6)$$

where  $\beta$  describes the rise time of the pulse and  $u(t)$  is the unit step function which takes on the value 1 for the duration of the pulse and is 0 otherwise.

Further effects which may distort the observed data include synchrotron radiation from the galactic background. Such radiation has a steep frequency dependence ( $\nu^{-2.6}$ ) and appears as a contributing factor in the total system temperature. This occurrence is particularly noticeable for frequencies below 5 GHz. Similarly, the ionosphere can impart an additional time and phase delay which becomes a factor especially in interferometric arrays. Inhomogeneous clumps in the ionosphere contribute to differential delays which are difficult to account for and calibrate (Stappers et al. 2011).

## 2.4. Pulsar Glitches

Glitches manifest as changes in the rotation rate of the pulsar. The rate of rotation suddenly increases over a short period of time, and is followed by a gradual relaxation to its original rotation frequency. These curious glitches are thought to arise due to a transfer

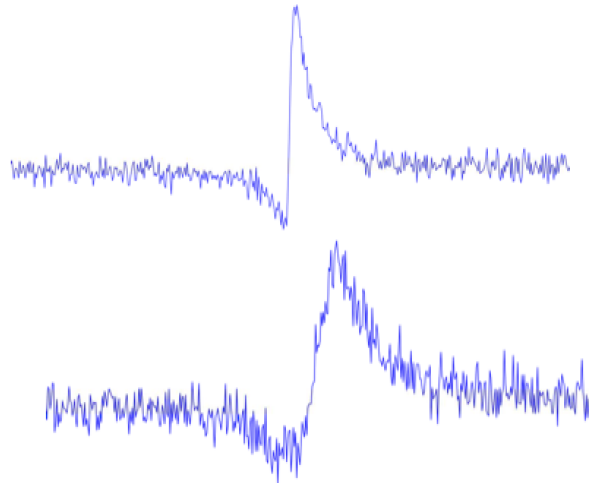


**Fig. 6.—:** A pulse observed in the 76 (*top*) and 60 MHz (*bottom*) passbands simultaneously. Broadening increases as the frequency decreases.

of angular momentum between the interior superfluid and the exterior crust of the neutron star as the two regions move at varying speeds relative to one another. The magnetosphere of the pulsar exerts an electromagnetic drag on the crust while the underlying superfluid continues to rotate unimpeded. The transfer of angular momentum between the two regions is demonstrated by a sudden glitch (Espinoza et al. 2011).

Pulsar glitches are generally observed as a timing residual between the pulse time-of-arrival and the arrival time predicted based on parameters such as the pulsar’s rotation and orbit, for instance (Espinoza et al. 2011). The ultimate determination of a pulsar glitch is therefore an exercise in pulsar timing.

### 3. Emission Mechanism

The Crab Pulsar serves as an invaluable astrophysical probe for its characteristic emission across the spectrum of wavelengths. The nature of the emission mechanisms responsible for the radiation remains a topic of uncertainty, however. Furthermore, it is critical to consider the possibility of varying mechanisms for discrete wavelengths and their corresponding energies. As we will see, the processes responsible for giant radio pulses at low frequencies

differ from those that result in emission at much higher frequencies.

### 3.1. High Energy Radiation

There are currently several existing theories that describe the mechanisms for high energy radiation from the Crab. One such proposed mechanism is that of curvature radiation. Curvature radiation occurs as relativistic electrons travel along curved magnetic field lines (Carroll & Ostlie 2007). In the magnetospheric plasma where large values of  $\mathbf{E} \cdot \mathbf{B}$  exist, electron-positron pair production occurs as the primary photons created via curvature radiation collide with X-rays (Cheng et al. 1986b). The X-rays themselves are created via synchrotron radiation, in which relativistic electrons spiral around the magnetic field lines. These X-rays undergo inverse Compton scattering off the same electron-positron pairs to produce  $\gamma$ -rays. Inverse Compton scattering occurs as photons scatter off of electrons and gain energy, resulting in shorter wavelength photons. The high energy radiation observed from the Crab is due to the creation of X-rays from synchrotron radiation and the production of  $\gamma$ -rays from inverse Compton scattering (Zhang & Cheng 1997).

### 3.2. Giant Radio Pulses

The emission mechanism responsible for producing the high intensity giant radio pulses differs depending on whether the pulse is a MP or IP. Careful analysis of the pulse profiles (described in Section 2.2) can lead to an increased understanding of the specific processes taking place at the emitting region.

The observed microbursts within the MP of the Crab may provide information regarding the small-scale structure of the regions of the magnetospheric plasma responsible for GRPs. Currently, several models have been proposed explaining the occurrence of microbursts. One such model posits that curvature radiation dominates in the region of the light cylinder where magnetic field lines remain open. Here, long, filament-like beams radiate away from the star. As these beams rotate in and out of the line of sight, radiation is periodically observed. The relation of microbursts to this phenomenon is believed to be inherent in the angular size of the radiating beam. A similar model suggests clusters, or clouds, of accumulated charge that

occasionally move across the radiating beams. Giant radio pulses are then observed when these clouds are within the beam and along the line of sight to the observer (Crossley et al. 2010).

Just as microbursts can illuminate the nature of the emitting radiation, the nanoshots that comprise them can be equally revealing. Due to the short duration and narrow bandwidth of several observed individual nanoshots, another proposed radiation mechanism is soliton collapse in strong plasma turbulence, where solitons are defined as self-reinforcing wave packets that can maintain their shape even as they move through a dispersive medium (Mikhailovskii et al. 1985). The implications of such a mechanism suggest an inhomogeneous magnetospheric plasma that is continuously changing as a function of time. Such irregularities in the pulsar plasma can exist only when the charge density differs from the Goldreich-Julian density (Eq. 1). When a charge density  $\rho \neq \rho_0$  exists, large potential differences in the electric field occur. These potential differences lead to ongoing fluctuations in the charge density which prohibit the plasma from maintaining a steady state. The resulting effect is that plasma waves are converted into electromagnetic waves that are free to escape from the plasma (Hankins & Eilek 2007b).

An important point of note is that the majority of theoretical models explaining GRPs are not based directly on observational data, in that they cannot reproduce the observed phenomena precisely. Currently, the only existing model which is able to do so is the Lyutikov model. This particular model rests on the notion of Alfvén waves. Alfvén waves occur as a product of the interaction between electric currents within magnetic field lines. The tension of the magnetic field lines acts as a restoring force, causing ions to oscillate about the lines while propagating in the forward direction (Lyutikov 2007).

The Lyutikov model deviates surprisingly from other currently existing models in that it requires a plasma density substantially greater than the Goldreich-Julian density proposed in Eq. 1 above; a density approximately  $10^5$  times the Goldreich-Julian density is suggested to define the magnetosphere within the closed field lines of the magnetic field. Assuming a density  $3 \times 10^4$  times the Goldreich - Julian density, the emission bands observed by Hankins & Eilek were successfully reproduced (see Lyutikov 2007 for details).

## 4. Data Analysis

### 4.1. Instrumentation – LWA1

The first Long Wavelength Array station (LWA1) is co-located with the Very Large Array (VLA) approximately 50 miles west of Socorro. This station is the first of a 53 station array that will be spread across New Mexico forming a large aperture synthesis imaging array. It consists of 260 dual-polarized dipole antennas arranged over a 100 m x 110 m collecting area, where five of these antennas lie beyond the perimeter and serve as outriggers. The longer elongation lies in the North-South direction which allows for the preservation of main lobe symmetry at lower declinations. The antennas themselves are distributed in a pseudo-random array in order to reduce sidelobes.

The LWA1 operates between 10 and 88 MHz. The dipoles are individually digitized and combined to form four dual polarized beams with independent pointings via a delay-sum beamforming technique. Each beam offers two tunings with an effective bandwidth of 16 MHz. In addition to beamforming, the LWA1 also has two transient buffer modes in which all dipoles observe the entire sky simultaneously. For an in-depth discussion of LWA1, see Ellingson et al. (2013b).

### 4.2. Observations

We observed the Crab Pulsar for a total of 100 hours over a period of seven months with the LWA1. The giant pulses discussed here are from 65 of the total hours. Many of the remaining hours simply require reprocessing, while some resulted in faulty data. Each hour of data corresponds to 512GB. The observations consisted of two separate beams with two frequency tunings per beam. The center frequencies were 76, 60, 44, and 28 MHz, with a usable bandwidth of about 16 MHz per tuning. The observations were conducted in split-bandwidth mode. As a result, signals below 30 MHz are attenuated, mitigating low frequency radio interference (RFI). This resulted in essentially continuous coverage of the pulsar from 20 - 84 MHz. This sample represents the largest survey to date of giant pulses at these low frequencies.

### 4.3. Data Reduction

The first step in the data reduction process was to convert the raw, beamformed digital receiver (DRX) voltages to the standard PSRFITS format (Hotan et al. 2004). This format is recognized by most pulsar processing pipelines, such as PSRCHIVE and PRESTO (see Ransom et al. 2002 and van Straten et al. 2012). The next step was to search for and mask RFI by identifying inconsistent signals in frequency and time. Regions that are identified as RFI are replaced by median values across the time gap. The output mask is used for subsequent data processing.

At this point in the reduction process, the data were analyzed via incoherent dedispersion. The effective smearing of a pulse across the entire bandwidth as the pulse is dispersed by the interstellar medium degrades the intrinsic time resolution of a pulse. As this effect becomes especially prevalent with decreasing frequencies, for low enough frequencies, a pulse can be smeared out entirely over the bandwidth. Incoherent dedispersion splits the entire bandwidth into channels. The amount of smearing across an individual channel is reduced by a factor that is directly proportional to the total number of channels. A large number of channels therefore mitigates the smearing of pulses and increases the overall time resolution. The signals from each channel are differentially delayed based on an assumed dispersion measure and subsequently combined to form a single dedispersed pulse. The Crab Pulsar has been known to exhibit variability in DM (see Rankin & Roberts 1971), and therefore dedispersion was performed over a range of DMs centered on the nominal DM value for the Crab. A fast fourier transform (FFT) was then performed on the time series and any remaining large scale time variations (red noise) were removed. Following red noise removal, a FFT was again performed on the resulting time series.

### 4.4. Identification of Giant Pulses

To extract giant pulses from the data, pulse-matched filtering was performed over each time series. In this process, a series of templates with varying characteristic broadening times were created and cross correlated with the signal. The template pulse shapes are defined by Eq. 6. Candidate pulses were subtracted from the time series and subsequent cross-correlations were performed.

This final step in the pipeline resulted in false positives on several occasions. As a result, only pulses adhering to the following criteria were included in the final list: For a given pulse, the SNR vs DM was plotted, where a gaussian-like peak near the Crab’s canonical DM was considered a pulse. Plots that were erratic, linear, or otherwise non-Gaussian in nature were discarded as RFI.

Matched filtering of the time series is difficult at these frequencies. Ionospheric scintillation causes variations in the noise base line of the time series that may obscure the pulse profile. This effect is most prevalent at the lowest frequencies in our band. RFI is also pervasive at these frequencies. Reflections from ionized meteor trails and low Earth orbiting satellites can result in dispersed signals on time scales similar to those seen in scattered pulses (Ellingson et al. 2013b). Consequently, the ultimate determination of pulses became a largely manual endeavor.

#### 4.5. Flux Calibration

The flux density of giant pulses is calibrated by considering the system equivalent flux density (SEFD) and the flux of Tau A (the nebula surrounding the Crab Pulsar). The latter is given by

$$S_{TauA} = (1944Jy)(\nu/76)^{-0.27} \quad (7)$$

where the spectral index was first constrained by Baars et al (1977). The SEFD represents the sensitivity of the receiver and the antenna. It typically varies as a function of frequency, local sidereal time (LST), and elevation angle. In order to calculate the SEFD, a number of drift scan observations of radio sources Cyg A, Cas A, and Tau A were taken (see Schinzel & Polisensky 2014). In each case, the source drifts through a fixed beam. The total peak power is measured as the source transits through the center of the beam ( $P_1$ ). The SEFD for Tau A is then given by

$$SEFD = S_{TauA} \left( \frac{P_1}{P_0} - 1 \right)^{-1} \quad (8)$$

where  $P_0$  is the off-peak power, measured when the source has not yet entered the side lobes. Based on the dependence of each SEFD on elevation angle, the values are normalized to derive a total SEFD value at zenith. For our observations at a given elevation angle  $E$ , we multiply the following power ratio fraction to our normalized SEFD to obtain the total SEFD in the direction of the Crab at the time of our observations (Stovall et al. 2014).

$$P(E) = 166.625 \times E^{-1.251} + 0.401 \quad (9)$$

Because our observations are limited to one hour in duration, variations in the SEFD due to shifting elevation angles are negligible. The flux densities for individual pulses are then calculated via the radiometer equation (Dewey et al. 1985). The error in the SEFD at zenith is approximately 20%. Including potential variations in SEFD with LST, we assume a total flux density error of about 40% (Stovall et al. 2014). We impose a  $4.4\sigma$  sensitivity threshold for all pulses. Figure 7 shows the distribution of flux densities for all pulses detected at 76 MHz. The brightest giant pulse detected corresponds to a peak flux of 107 kJy. It was detected in the 76, 60, and 44 MHz passbands simultaneously.

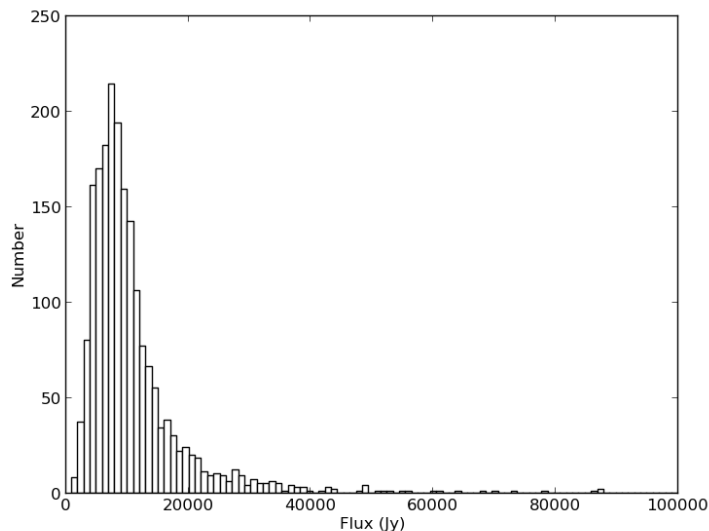


**Fig. 7.**—: Distribution of flux densities for all pulses observed at 76MHz.

## 5. Results & Discussion

In 65 hours of observations, 2,007 pulses were detected at 76 MHz, and 1,091 pulses were detected at 60MHz. The number of pulses detected at 44 and 28 MHz was significantly lower. These values are not thought to be representative of actual detection rates, however. Rather, these lower tunings were divided into fewer channels than are necessary in order to remove smearing and thereby detect a pulse. We intend to reprocess these observations at a later date. For the following discussion, statistics are concerned only with the highest tunings. Table 1 lists each date and respective detections per frequency band. Our detection rates are greater than those presented in Ellingson et al. (2013a) due to improved calibrations of LWA1 cable delays.

### 5.1. Occurrence of Giant Radio Pulses

The number of pulses per observation have been plotted over the 7 month period (See Figure 8). The apparent increase in the number of pulses over time cannot be attributed to instrumental effects. Figure 9 shows the results of drift scan observations of Cyg A which remain relatively constant over time, indicating no evident changes in system sensitivity. The slight variations in these drift scans are due to seasonal changes. Similarly, RFI conditions appear to be relatively stable.

One possible explanation for the gradual increase in the number of pulses over time may be pulsar glitches, as discussed in section 2.4. If the rotation rate of the Crab has increased over some period of time, we would expect to see a greater flux of pulses over the same observing time. Furthermore, there are no known correlations between the radio flux density of pulses and glitches. As Figure 8 shows, although the number of pulses increases, the flux densities remain relatively stable. Recent followup observations of the Crab were taken, in which the number of pulses per hour have relaxed to their original rates, which is also indicative of a possible glitch. We intend to continue monitoring the Crab in order to determine any further trends in the number of pulses detected.

Because it is difficult to detect the main pulses of the Crab at low frequencies (due to scattering), we cannot definitively determine whether or not a glitch has occurred. Therefore,

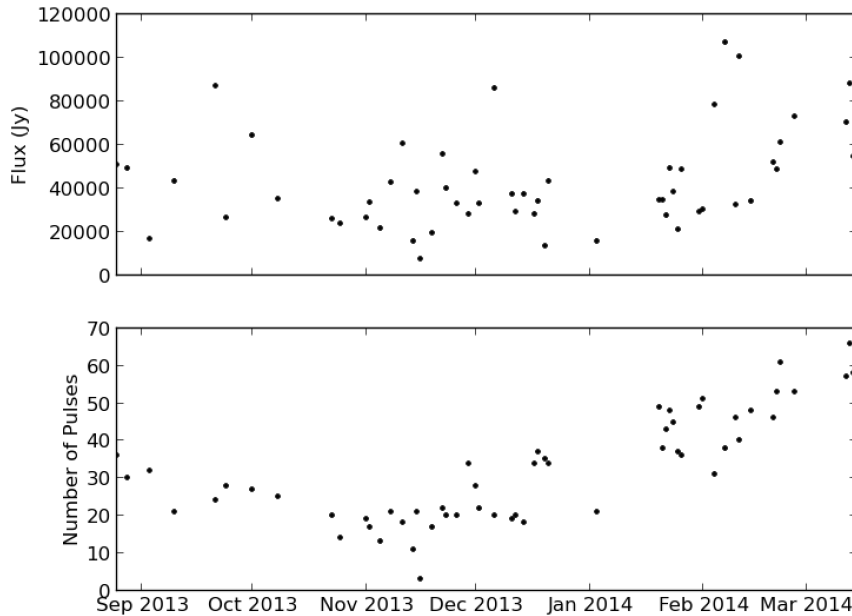


**Fig. 8.**—: *Top:* Highest flux density pulses per day at 76MHz. *Bottom:* Number of pulses per day at 76MHz.

detection of a glitch is contingent on potential simultaneous pulsar timing observations at higher frequencies. At this time, we can think of no other possible explanations for the increase in the number of giant pulses detected.

## 5.2. Variations in DM

Because incoherent dedispersion was performed over a range of DMs, we found that the highest signal-to-noise pulses were spread across DMs. Figure 10 shows the distributions. These variations can perhaps be attributed to line-of-sight crossings by filaments in the nebula, as discussed above. Similarly, the solar wind has been known to impart DM variations, as can turbulent spatial variations in the interstellar medium (You et al. 2007). A closer examination of the timescale of variations is necessary in order to differentiate between possible causes. For example, shorter timescales are likely indicative of filaments within the nebula itself.

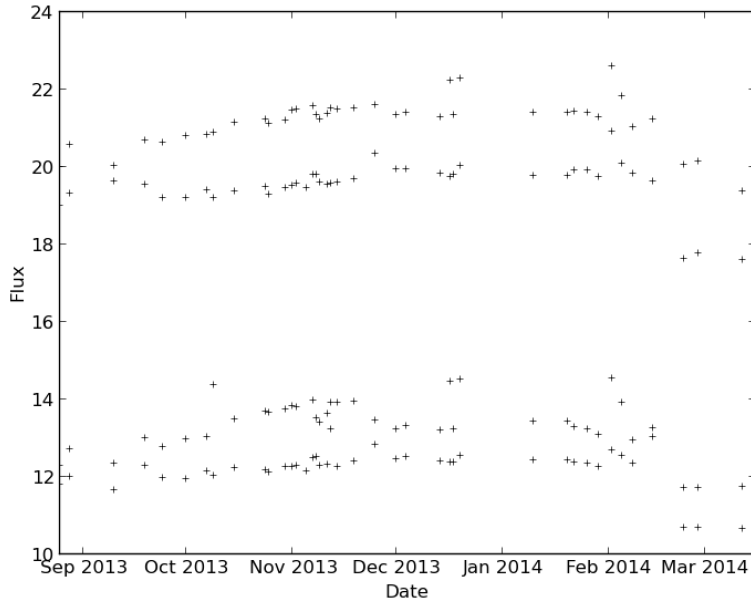


**Fig. 9.**—: *Top*: Drift-scan observations of Cyg A. Shown are (from top to bottom), 65 MHz - Y polarization, 65 MHz - X, 75 MHz - Y, and 75 MHz - X.

### 5.3. Characteristic Broadening Time

Mean values for the characteristic broadening times for various studies have been plotted in Figure 11. Values from this study represent upper limits. Table 2 lists all values plotted, where the values from this study are the mean values and therefore not the values depicted in the plot. We have simply plotted upper limits in the place of mean values with  $1\sigma$  error bars, as our standard deviations are large, likely due to an error in the search method. Further refinement in our search method is therefore required in order to obtain accurate error measurements, however we believe our mean values to be accurate. Broadening times for this study correspond to pulse-matched filters with the highest signal to noise. In the case of a Kolmogorov spectrum, the dependency is given by  $\tau_d \propto \nu^{-4.4}$ , as discussed above. A log-linear least squares fit to the data in Figure 11 (including mean values from this work) gives  $\tau_d \propto \nu^{-3.4}$ . If previous  $\tau_d$  values as measured with LWA1 and presented in Ellingson et al. (2013a) are removed, the resulting power law dependence is given by  $\tau_d \propto \nu^{-3.1}$ . These dependencies are comparable to the one reported by Karuppusamy et al. (2012),  $\tau_d \propto \nu^{-3.2} \pm 0.1$ . This deviation from the Kolmogorov spectrum may suggest the intrinsic

nature of the magnetosphere from which pulses are emitted. Since our low frequency values are consistent with observations at a range of other frequencies, these results can be used to further constrain the turbulence of the pulsar magnetosphere.

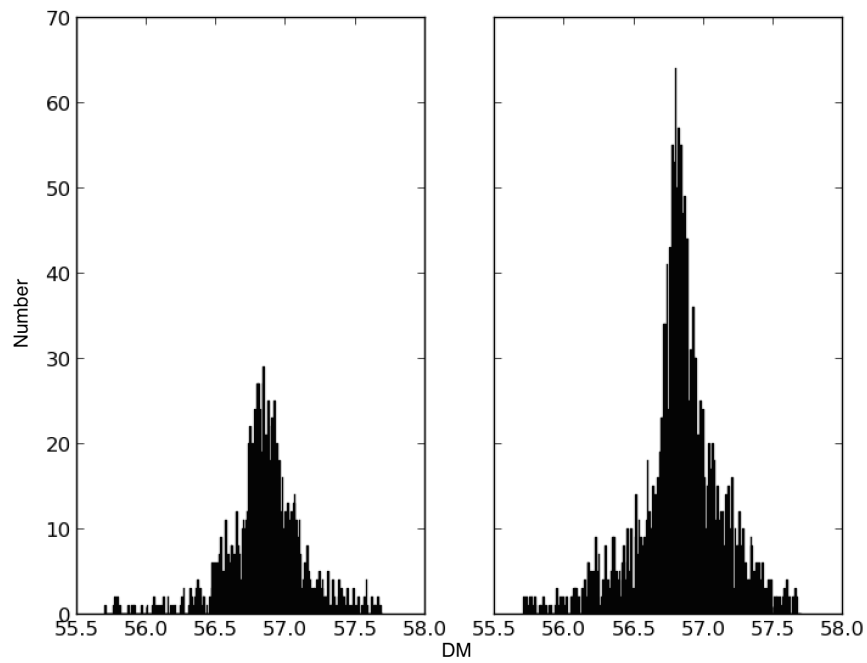


**Fig. 10.**—: Spread of DMs from highest SNR pulses for 64MHz (*Left*) and 74MHz (*Right*), respectively.

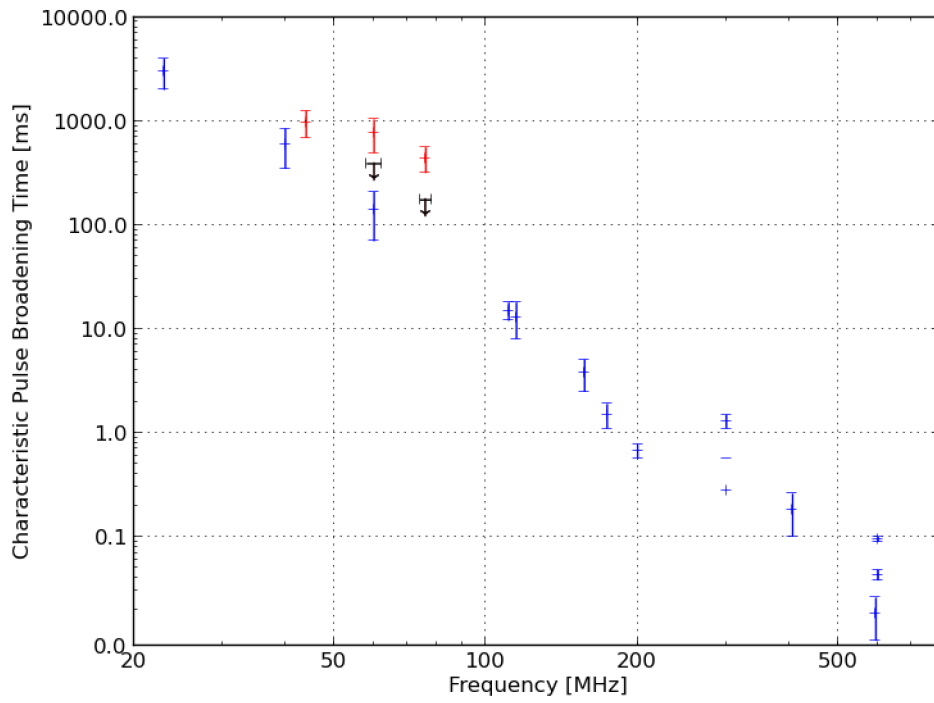


**Fig. 11.**—: Characteristic pulse broadening times  $\tau_d$  from other studies (blue), Ellingson et al. (2013) (red), and upper limits for this study (black). The error bars represent  $\pm 1\sigma$  from the mean.

MJD	44MHz	60MHz	76MHz	$S_{76}[kJy]$
056526	–	11	36	50.7
056529	1	–	30	49.2
056538	0	–	32	17.0
056545	–	17	21	43.5
056556	2	19	24	87.1
056559	–	19	28	26.7
056566	13	18	27	64.5
056573	–	11	25	35.2
056580	–	13	15	15.7
056588	7	15	20	26.0
056589	–	17	26	15.9
056590	3	13	14	23.8
056595	1	7	12	16.0
056596	2	16	19	20.4
056597	2	15	19	26.7
056598	4	19	17	33.6
056601	3	–	13	21.9
056603	1	1	4	42.8
056604	3	17	21	43.0
056605	2	16	25	26.1
056607	1	–	18	60.3
056608	0	17	37	22.9
056610	1	11	11	15.7
056611	6	17	21	38.7
056612	1	3	2	7.9
056615	5	20	17	19.6
056618	0	15	22	55.8
056619	5	16	20	40.2
056622	2	15	20	33.4
056625	–	19	34	28.0
056627	–	13	28	47.8
056628	–	11	22	33.3
056632	3	13	20	86.0
056637	1	16	19	37.7
056638	0	16	20	29.2
056640	1	7	18	37.3
056643	–	25	34	28.5
056644	–	16	37	34.0
056646	–	23	35	13.7
056647	–	17	34	43.4
056660	–	15	21	16.0
056677	0	26	49	34.7
056678	–	29	38	34.7
056679	0	21	43	27.7
056680	–	24	48	49.0
056681	0	31	45	38.4
056682	–	15	37	21.1
056683	–	26	36	49.9
056688	2	20	49	29.1
056689	1	39	51	30.3
056692	–	25	31	79.6
056695	7	29	38	107.0
056698	–	14	46	32.8
056699	0	32	40	100.4
056702	0	8	48	34.2
056708	–	32	46	52.1
056709	2	38	53	48.7
056710	–	47	61	61.3
056711	4	32	53	73.1
056728	–	39	57	70.3
056729	–	9	66	87.8
056730	0	29	58	54.7
056731	–	12	58	42.8
056946	–	–	25	31.5
056974	–	–	10	27.5

**Table 1::** Number of giant radio pulses detected per date in each frequency band. Column 5 lists the highest flux density pulses at 76 MHz per day.

$\nu$ [MHz]	$\tau_d$ [ms]	Reference
23	$300 \pm 1000$	Popov et al. (2006)
40	$600 \pm 250$	Kuzmin et al. (2002)
44	$978 \pm 287$	Ellingson et al. (2013)
60	$140 \pm 70$	Kuzmin et al. (2002)
60	$768 \pm 273$	Ellingson et al. (2013)
60	$48 \pm 324$	<i>This work</i>
76	$439 \pm 122$	Ellingson et al. (2013)
76	$31 \pm 147$	<i>This work</i>
111	$15 \pm 3$	Popov et al. (2006)
115	$13 \pm 5$	Staelin & Sutton (1970)
157	$3.8 \pm 1.3$	Staelin & Sutton (1970)
174	$1.5 \pm 0.4$	Karuppusamy et al. (2012)
200	$0.670 \pm 0.100$	Bhat et al. (2007)
300	$1.3 \pm 0.2$	Sallmen et al. (1999)
300	0.28	Sallmen et al. (1999)
406	$0.18 \pm 0.08$	Kuzmin et al. (2002)
594	$0.018 \pm 0.008$	Kuzmin et al. (2002)
600	$0.095 \pm 0.005$	Sallmen et al. (1999)
600	$0.043 \pm 0.005$	Popov et al. (2006)

**Table 2::** Characteristic pulse broadening times  $\tau_d$  from various measurements as in Ellingson et al. (2013), modified to include measurements from this work. The two values at 300 MHz for Sallmen et al. (1999) represent different scattering epochs.

## 6. Conclusion and Future Work

This survey represents the largest sample of giant pulses observed at these frequencies. Over 2,000 pulses have been detected; we hope to increase this number with further analysis of the remaining data. Our observations of the characteristic scattering time are consistent with other studies and indicate that the turbulence of the pulsar magnetosphere may be affecting observed pulse widths. These results can therefore be utilized in an attempt to further constrain the nature of the magnetosphere. In addition, the curious trend in the number of pulses detected over time may be indicative of pulsar glitches, a poorly understood phenomenon. Our results therefore provide a unique glimpse into the low frequency nature of the Crab pulsar. Combining these results with those at higher frequencies will help reveal the nature of pulsar emission mechanisms.

Future work will include incorporating the lower frequency tunings with our current statistics. In addition, we are continuously monitoring the Crab in an attempt to better constrain variations in the number of giant pulses emitted. We also plan to observe the Crab simultaneously at higher frequencies such as the optical. Finally, we will continue to explore automated methods for detecting Crab giant pulses at low frequencies.

While giant radio pulses are a phenomenon reserved for but a few pulsars, a greater understanding of the emission mechanisms which lead to these high-intensity bursts can help us better understand the overarching conditions at a rotating neutron star. Such conditions are inherently valuable in understanding emission across the spectrum of wavelengths. Current theories regarding GRP emission are largely speculative. However, as more observations arise and new details emerge, our ability to reproduce the observed phenomena increases. Further studies at low frequencies are necessary in order to reach affirmative conclusions regarding these processes.

As our detection methods improve, the search for giant radio pulses will lend itself to searching for other transient radio sources in our galaxy and beyond. Perhaps high intensity radio objects and events lay waiting in the vast reaches of space for our telescopes to catch a glimpse of the stories they tell.

I would like to thank my supervisor, Dr. Greg Taylor, for his guidance and support, and for the opportunity to explore the mysterious Crab Pulsar. I would also like to thank Dr. Kevin Stovall for his vital contributions to this project.

Construction of the LWA has been supported by the Office of Naval Research under Contract N00014-07-C-0147 and by the Air Force Office of Scientific Research DURIP program. Support for operations and continuing development of the LWA1 is provided by the National Science Foundation under grants AST-1139963 and AST-1139974 of the University Radio Observatory program.

“Somewhere, something incredible is waiting to be known.” – Carl Sagan

## REFERENCES

- Apparao, K.M.V. 1974, *Astrophys. Space Sci.* 31, L9
- Baars, J.W.M. et al. 1977, *Astron. Astrophys.*, 61, 99
- Brentjens, M.A. & A. G. de Bruyn 2005, *A&A*, 441, 1217
- Carroll, B.W. & Ostlie, D.A. *An Introduction to Modern Astrophysics*, Pearson Education, Inc. 2007
- Cheng et al. 1986a, *ApJ*, 300, 500
- Cheng K. S., Ho C., Ruderman M., 1986b, *ApJ*, 300, 522
- Cronyn, W.M. 1970, *Science, New Series*, Vol. 168, No. 3938, 1453-1455
- Crossley, J.H. et al. 2010, *ApJ*, 722, 1908
- Dewey, R. J., Taylor, J. H., Weisberg, J. M., Stokes, G. H. 1985, *ApJ*, 294, L25
- Ellingson, S. W. et al. 2013a, *ApJ*, 768, 136
- Ellingson, S. W., et al. 2013b, *IEEE Transactions on Antennas and Propagation*, 61, 2540
- Espinoza, C.M. et al. 2011, *MNRAS* (2011) Vol. 414 1679-1704
- Gedlain, M. et al. 1998, *Phys. Rev. E*, 57, 3399-3410
- Goldreich, P., and Julian, W. H. 1969, *ApJ* , 157, 869
- Hankins, T.H. and Eilek, J.A. 2007a, *AAS, Bulletin of the American Astronomical Society*, Vol. 39, p.918
- Hankins, T. H., Eilek, J. A. 2007b, *ApJ*, 670, 693
- Hankins, T.H. et al. 2003, *Nature*, 422, 141
- Hankins, T.H. et al. 2010, *Astro2010 Science Frontier Panel, Stars and Stellar Evolution*
- Hotan, A.W. et al. 2004, *Publications of the Astronomical Society of Australia*, 21(3), pp. 302-309
- Isaacman, R., & Rankin, J.M. , 1977, *Astrophys. J.* 214, 214
- Jensen, E. A. et al. 2010. *Solar Physics*, 265(1), pp 31-48
- Jessner, A. et al. 2005, *Advances in Space Research*, 35

- Karuppusamy, R., Stappers, B.W. Lee, K.J. 2012, *Astronomy & Astrophysics*, 538, A7
- Karuppusamy, R., Stappers, B. W., and van Straten, W. 2010, *A&A*, 515, A36
- Lang, K.R. 1971, *ApJ*, 164, 249
- Lyutikov, M. 2007, *MNRAS*, 381
- Mayall, N.U. 1939, *ASPL*, 3, 145
- Michailovskii, A.B. et al. 1985, *Fizika Plasmy*, 11, 369
- Petrova, S. A. 2004, *A&A*, 424, 227
- Rankin, J.M. Roberts, J.A. 1970. In: Davies R.D., Smith F.G. (eds.) *Proc. IAU Symp. 46, The Crab Nebula*. Reidel, Dordrecht, 114
- Ransom, S.M. et al. 2002, *The Astronomical Journal*, 124: pp1788-1809
- Schinzl, F., Polisensky, E. 2014, *LWA Memo Series*
- Staelin, D.H. and Reifenshtein, E.C. 1968, *Science, New Series*, Vol. 162, No. 3861, 1481-1483
- Stappers, B.W. et al. 2011, *A&A*, 530, A80
- Stovall, K. et al. 2014, *arXiv:1410.7422*
- Sotomayor-Beltran, C., Sobey, C., Hessels, J. W. T., et al. 2013, *AA*, 552, A58
- Vandenberg, N.R. 1976, *Astrophys J.* 209, 578
- van Straten, W. et al. 2012, *Astron. Res. and Technol.*, 9, 237
- You, X. P. et al. 2007, *Mon. Not. R. Astron. Soc.* 378, 493-506
- Zhang, L. & Cheng, K.S. *Astrophysical Journal Letters*, 1997, v. 487, p. 370-379